PAPER

TiO₂/graphene/NiFe-layered double hydroxide nanorod array photoanodes for efficient photoelectrochemical water splitting†

Fanyu Ning, Mingfei Shao,* Simin Xu, Yi Fu, Ruikang Zhang, Min Wei,* David G. Evans and Xue Duan

The ever-increasing demand for renewable and clean power sources has triggered the development of novel materials for photoelectrochemical (PEC) water splitting, but how to improve the solar conversion efficiency remains a big challenge. In this work, we report a conceptual strategy in a ternary material system to simultaneously enhance the charge separation and water oxidation efficiency of photoanodes by introducing reduced graphite oxide (rGO) and NiFe-layered double hydroxide (LDH) on TiO₂ nanorod arrays (NAs). An experimental–computational combination study reveals that rGO with a high work function and superior electron mobility accepts photogenerated electrons from TiO₂ and enables fast electron transportation; while NiFe-LDH acts as a cocatalyst which accelerates the surface water oxidation reaction. This synergistic effect in this ternary TiO₂/rGO/NiFe-LDH photoanode gives rise to a largely enhanced photoconversion efficiency (0.58% at 0.13 V) and photocurrent density (1.74 mA cm⁻² at 0.6 V). It is worth mentioning that the photocurrent density of TiO₂/rGO/NiFe-LDH, to the best of our knowledge, is superior to previously reported TiO₂-based photoanodes in benign and neutral media. In addition, the method presented here can be extended to the preparation of other efficient photoanodes (WO₃/rGO/NiFe-LDH and α-Fe₂O₃/rGO/NiFe-LDH) toward high level PEC performance.

Broader context

Photoelectrochemical (PEC) water splitting has become one of the most important approaches for solar energy conversion and chemical fuel production, but its solar-to-hydrogen conversion efficiency normally suffers from poor charge carrier mobility and sluggish reaction kinetics of photoelectrodes. Herein we report the design and fabrication of a ternary material system by introducing reduced graphite oxide (rGO) and NiFe-layered double hydroxide (LDH) onto TiO₂ nanorod arrays (NAs) for largely enhanced PEC performance. An experiment–calculation combination study reveals that rGO with a high work function and superior electron mobility accepts photogenerated electrons from TiO₂ and enables fast electron transportation, while NiFe-LDH acts as a cocatalyst which captures photogenerated holes and accelerates the surface water oxidation reaction. Consequently, the resulting TiO₂/rGO/NiFe-LDH NAs photoanode generates a photocurrent density of 1.74 mA cm⁻² at 0.6 V *vs.* SCE, which achieves 93% of the theoretical limit of TiO₂. This is, to the best of our knowledge, superior to those of previously reported TiO₂-based photoanodes in benign and neutral media.

1. Introduction

With the increasing exploration and development of renewable and clean power sources, photoelectrochemical (PEC) water splitting into hydrogen and oxygen using solar energy have

State Key Laboratory of Chemical Resource Engineering,
Beijing University of Chemical Technology, Beijing 100029, P. R. China.
E-mail: shaomf@mail.buct.edu.cn, weimin@mail.buct.edu.cn;
Fax: +86-10-64425385; Tel: +86-10-64412131
† Electronic supplementary information (ESI) available: Experimental and computational details and supplementary figures and tables are included. See DOI: 10.1039/c6ee01092j

attracted considerable attention.[1–3] The PEC water splitting process which integrates solar energy conversion and water electrolysis in a single photoelectrode involves several reaction steps: the generation of electron–hole pairs by absorbed photons, the separation and migration of charges to the electrode interface, and the surface water oxidation/reduction reaction with holes/electrons.[4,5] An efficient solar-to-hydrogen conversion indicates that all these sequential steps are achieved smoothly, which requires the electrode materials to simultaneously satisfy multiple requirements. Semiconductor photocatalysts, in particular transition-metal oxides such as TiO₂,[6–8] α-Fe₂O₃,[9–11] and WO₃,[12,13] have been extensively studied as photoanode materials for PEC

This journal is © The Royal Society of Chemistry 2016

Energy Environ. Sci., 2016, **9**, 2633–2643 | 2633

water splitting with low cost and environmental-friendliness. However, these photoelectrodes normally suffer from poor charge carrier mobility[3,14,15] and large kinetic barriers for surface water oxidation,[4,16,17] which results in unsatisfactory photoconversion efficiency.

The fabrication of composite photoelectrodes with appropriate composition and well-designed nanostructure gives a promising route for improving the PEC performance.[9] For instance, the charge separation can be effectively facilitated by the construction of semiconductor heterojunctions with matched band edge positions (*e.g.*, TiO_2/CdS QDs,[18] α-Fe_2O_3/Si,[19] and WO_3/$BiVO_4$[20]) or the incorporation of a conducting medium (*e.g.*, CNTs and graphene[21–24]). Particularly, due to its unique atomic-thick 2D structure and excellent physicochemical properties, graphene has inspired great interest in photocatalysis and PEC water splitting.[22] When combined with semiconductors (TiO_2, Fe_2O_3, and $BiVO_4$), graphene can act as an electron shuttle which induces photogenerated electron transfer from the conduction band of the semiconductor to graphene due to its higher work function.[22–28] To enhance the surface reaction kinetics, oxygen evolution reaction (OER) cocatalysts (*e.g.* IrO_x,[29] CoO_x,[30] and FeOOH[31]) have been introduced to provide new reaction pathways with decreased kinetic barriers. Recently, NiFe-layered double hydroxide (LDH) materials have shown surprisingly high OER performances,[32,33] which may serve as promising candidates for PEC water oxidation cocatalysts. Previous studies also reported ingenious photoelectrodes with improved PEC performance by fabricating various nanostructures (*e.g.*, porous films,[23,34] ordered nanowire arrays,[8,14] and core–shell nanoarrays[20,28]). In spite of all this progress, a simultaneous improvement in separation/migration of photogenerated charge carriers as well as the surface reaction kinetics is highly desirable for efficient PEC water splitting; a study on the synergistic effect of each component and the reaction mechanism remains a big challenge. Such detailed information and understanding are valuable in the rational design and preparation of new PEC photoelectrodes with largely enhanced performance.

Herein, we report the design and fabrication of well-aligned nanorod array (NA) photoanodes by spin-coating of graphene nanosheets on the surface of TiO_2 NAs, followed by a subsequent electrodeposition of NiFe-layered double hydroxide (LDH) nanoplatelets, which exhibit largely enhanced PEC water splitting performances. Hierarchical TiO_2/rGO/NiFe-LDH NAs with a core–shell structure are demonstrated with fine control over the composition and morphology; rGO and LDH nanoplatelets are uniformly anchored onto the surface of TiO_2 NAs. The resulting ternary NAs display excellent performance for PEC water splitting with largely enhanced photoconversion efficiency (2.6 times higher than that of pristine TiO_2) and satisfactory stability (97% retention of photocurrent within 3 h test). The experiment–DFT calculation reveals that the PEC enhancement of TiO_2 is attributed to the synergistic effect of the superior charge separation efficiency facilitated by rGO and the excellent water oxidation activity resulting from NiFe-LDH. Moreover, this strategy is also demonstrated in other ternary NA photoelectrodes with promising PEC water splitting performance.

2. Results and discussion

2.1 Material characterization

As a typical presentation, TiO_2 nanorod arrays (NAs) are chosen as a prototype for the investigation of the synergetic effect of graphene and NiFe-LDH, and Fig. 1A depicts the fabrication process of TiO_2/rGO/NiFe-LDH photoanodes. Vertically aligned TiO_2 NAs was firstly grown on a fluorine-doped tin oxide (FTO) substrate *via* a previously reported hydrothermal method,[35] with a diameter range from 100 to 150 nm and an average length of ∼2.5 μm (Fig. 1B and F). Subsequently, GO nanosheets (∼1.0 nm in thickness; Fig. S1, ESI†) were spin-coated onto TiO_2 NAs, followed by an annealing process in N_2 for a strong adhesion. It is found that the flexible rGO nanosheets are irregularly attached to TiO_2 nanorods with somewhat coverage on the top of the NAs (Fig. 1C, G and J). Finally, NiFe-LDH nanoplatelets with an average lateral size of ∼140 nm and a thickness of ∼9 nm are uniformly electrodeposited on the surface of the TiO_2/rGO NAs (Fig. 1D). A cross-section SEM image shows that the NiFe-LDH nanoplatelets are homogeneously distributed on the whole NAs (Fig. 1H). A TEM image further reveals the hierarchical core–shell morphology of the TiO_2/rGO/NiFe-LDH NAs (Fig. 1K). The composition and element distribution are further characterized. A Ti/C/Ni/Fe molar ratio of 16.31 : 2.05 : 0.87 : 0.68 is obtained from energy dispersive X-ray (EDX) spectroscopy (Fig. S2, ESI†). In addition, EDX mapping illustrates uniform signals for Ti, O, C, Ni, and Fe elements (Fig. 1L), which demonstrates the homogeneous distribution of rGO and NiFe-LDH on the TiO_2 NAs. As a control sample, TiO_2/NiFe-LDH core–shell NAs without rGO were synthesized by a direct electrodeposition of NiFe-LDH on the surface of TiO_2 nanorods (Fig. 1E and I). It is observed that the electrodeposited NiFe-LDH nanoplatelets in the TiO_2/rGO/NiFe-LDH NAs are more condensed with a larger lateral size compared with those in the pristine TiO_2 system under the same preparation conditions. This is attributed to the enhanced conductivity provided by rGO, which may facilitate the electrosynthesis of NiFe-LDH.

The composition and phase structure of these obtained NAs were investigated by XRD and Raman spectra. As shown in Fig. 2A, two sharp reflections located at 36.1° and 62.8° correspond to the (101) and (002) diffraction peaks of rutile TiO_2 (JCPDS No. 21-1276), respectively. No other reflection of rutile is observed, indicating the oriented growth of TiO_2 NAs with respect to the substrate.[36] The absence of the typical diffraction peaks of rGO is mainly due to its small loading amount. After the electrodeposition of NiFe-LDH, the (003) reflection of a typical LDH phase at 10.6° is observed. Raman spectra show the vibrational modes of rutile TiO_2 at ∼240 cm^{-1}, 445 cm^{-1} and 608 cm^{-1} (Fig. 2B), which can be assigned to the second order effect (SOE), E_g and A_{1g}, respectively.[37] Two bands located at ∼1359 cm^{-1} (D band) and 1586 cm^{-1} (G band) are observed in TiO_2/rGO and TiO_2/rGO/NiFe-LDH NAs, demonstrating the presence of rGO. The TiO_2/rGO and TiO_2/rGO/NiFe-LDH display an obviously decreased intensity ratio of D to G band (I_D/I_G = 0.82 and 0.81, respectively) relative to pure rGO (I_D/I_G = 0.99, Fig. S3, ESI†),
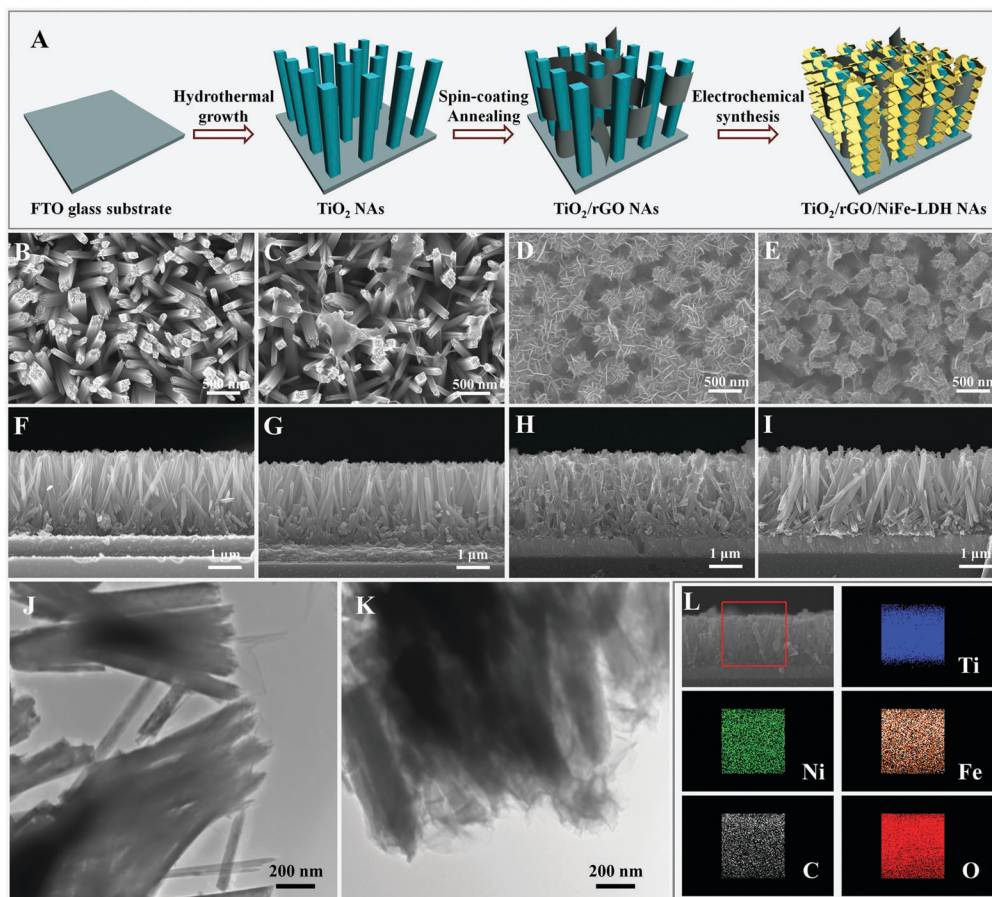
Fig. 1 (A) Schematic illustration for the fabrication of TiO$_2$/rGO/NiFe-LDH core−shell NAs; SEM images of (B and F) TiO$_2$ NAs, (C and G) TiO$_2$/rGO NAs, (D and H) TiO$_2$/rGO/NiFe-LDH NAs, and (E and I) TiO$_2$/NiFe-LDH NAs; TEM images of (J) TiO$_2$/rGO NAs and (K) TiO$_2$/rGO/NiFe-LDH NAs; and (L) EDX mapping of TiO$_2$/rGO/NiFe-LDH core−shell NAs.
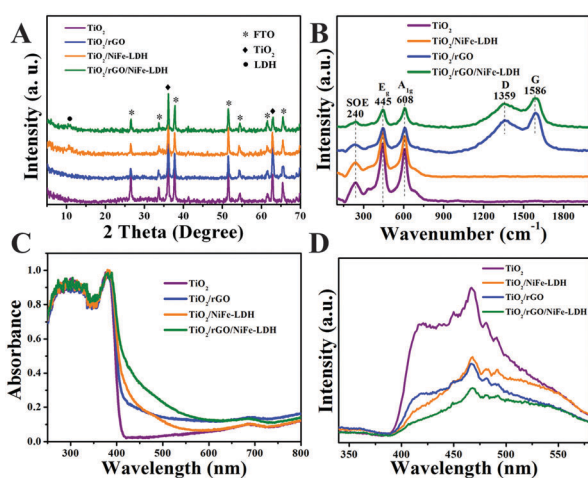

Fig. 2 (A) XRD patterns, (B) Raman spectra, (C) UV-Vis diffuse-reflectance spectra, and (D) PL spectra of TiO$_2$, TiO$_2$/NiFe-LDH, TiO$_2$/rGO, and TiO$_2$/rGO/NiFe-LDH NAs, respectively.

which is assigned to the high crystallinity of rGO with reduced surface defects in these NAs.[38] Moreover, a negative shift of the G band position (from 1596 cm^{-1} to 1586 cm^{-1}) is found after

the incorporation of rGO with TiO$_2$ or TiO$_2$/NiFe-LDH NAs, indicating an n-doping character of rGO with an electron transfer from TiO$_2$ to rGO in the composite material.[39]

The optical properties of these NA samples were investigated by UV-Vis diffuse reflectance spectroscopy and photoluminescence (PL) emission spectra. The TiO$_2$ NAs exhibit a strong absorption in the UV light region with a steep absorption edge at approximately 410 nm (Fig. 2C), and their band gap is calculated to be 3.11 eV (Fig. S4, ESI†). After the introduction of rGO and NiFe-LDH, absorbance in the visible light region increases gradually, owing to the visible light absorption of rGO and NiFe-LDH. This enhancement in visible light absorption originating from rGO is in accordance with previously reported graphene-based composites.[24,26,40] However, the enhanced visible light absorption does not represent an extended light response range for PEC water splitting which is sensitive to UV light. The correlation between light absorption and photocurrent conversion will be further discussed in the next section. The PL behavior, orginating from the recombination of photoinduced electron–hole pairs, can reflect the separation, migration and transfer of photogenerated charge carriers in semiconductors. As shown in Fig. 2D, TiO$_2$ NAs display rather strong PL emission peaks at ∼418 and 467 nm, which are attributed to the band gap transition and

This journal is © The Royal Society of Chemistry 2016

Energy Environ. Sci., 2016, **9**, 2633–2643 | **2635**

the charge transfer transition of oxygen vacancy trapped electrons, respectively.[41] The PL intensity of these two peaks decreases sharply after the incorporation of NiFe-LDH or rGO, and further declines in the ternary TiO_2/rGO/NiFe-LDH system. The decreased PL emission intensity indicates a significantly suppressed radiative recombination of photogenerated charge carriers, which benefits the electron–hole separation.[42,43] In addition, time-resolved PL spectroscopy (Fig. S5, ESI†) was carried out to investigate the dynamics of photogenerated charge carriers. By triple-exponential fitting of the emission decay curves (Table S1, ESI†), the fluorescence lifetime values are determined to be 8.06, 22.02, 28.68, and 28.05 ns for TiO_2, TiO_2/NiFe-LDH, TiO_2/rGO, and TiO_2/rGO/NiFe-LDH NAs, respectively. The prolonged fluorescence lifetime of TiO_2/rGO/NiFe-LDH is related to a long life of electrons in the excited state, which is highly desirable for the migration and surface reaction of photogenerated charge carriers.[44,45]

2.2 Enhanced PEC water splitting

PEC measurements were performed using TiO_2, TiO_2/rGO, TiO_2/NiFe-LDH, and TiO_2/rGO/NiFe-LDH NAs as photoanodes. Fig. 3A shows the linear sweep voltammograms (LSV), in which pristine TiO_2 NAs display a relatively low photoresponse over the whole potential window, with a photocurrent density of 0.92 mA cm^{-2} at 0.6 V (E_{RHE} = 1.245 V). In contrast, the TiO_2/NiFe-LDH NAs exhibit a cathodic shift of the onset potential from −0.2 V to −0.3 V, along with an increase in the photocurrent density (1.18 mA cm^{-2} at 0.6 V) compared with the pristine TiO_2 NAs. Despite some improvement, the PEC performance for the NiFe-LDH modified TiO_2 NAs is unsatisfactory probably due to the poor charge mobility of TiO_2/NiFe-LDH. For the TiO_2/rGO NAs, a largely enhanced photocurrent density (1.50 mA cm^{-2} at 0.6 V) with a similar onset potential to the pristine TiO_2 NAs is observed. In the case of the ternary TiO_2/rGO/NiFe-LDH NAs, a negatively shifted onset potential at −0.3 V is observed relative to the TiO_2/rGO NAs; the photocurrent density of 1.74 mA cm^{-2} at 0.6 V represents the highest value among these four photoanodes. Furthermore, the photoconversion efficiency of each photoanode was calculated based on the current–voltage curve as a function of applied voltage (Fig. 3B). The TiO_2/rGO/NiFe-LDH NA electrode shows a maximum photoconversion efficiency of 0.58% at 0.13 V, which is significantly larger than that of TiO_2/rGO (0.36%), TiO_2/NiFe-LDH (0.35%) and pristine TiO_2 (0.22%) at the same potential. The PEC performance of the ternary TiO_2/rGO/NiFe-LDH core–shell NAs clearly demonstrates a synergistic effect achieved by the integration of rGO and NiFe-LDH with TiO_2. It is worth mentioning that the photocurrent density of the TiO_2/rGO/NiFe-LDH NAs, to the best of our knowledge, is superior to reported TiO_2-based photoanodes (Table S2, ESI†) and also among the highest of other reported photoanodes in neutral medium.[16,21,28]

To further investigate the photoresponse of TiO_2, TiO_2/NiFe-LDH, TiO_2/rGO, and TiO_2/rGO/NiFe-LDH NAs, transient photocurrent measurements were carried out by LSV (Fig. 3C) and chronoamperometry (Fig. 3D) under chopped light illumination. As shown in Fig. 3C, all these samples display a prompt and reproducible photocurrent response with respect to the ON–OFF cycles of the irradiation signal. Amperometric I–t curves also depict the fast response toward irradiation stimulation. The current density of these electrodes under illumination follows a descending order as: TiO_2/rGO/NiFe-LDH > TiO_2/rGO > TiO_2/NiFe-LDH > pristine TiO_2 NAs. This is in high accordance with the LSV results (Fig. 3A) and further demonstrates the improvement in PEC performance provided by rGO and NiFe-LDH. Moreover, the square profiles and steady photocurrent density of transient photocurrent response in TiO_2/NiFe-LDH,
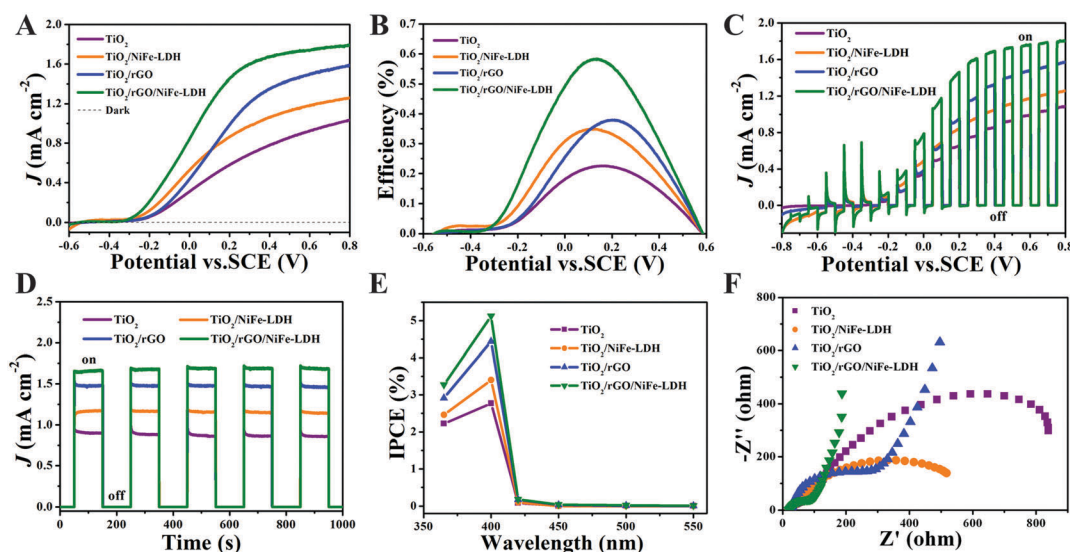

Fig. 3 (A) Current–voltage (J–V) curves, (B) calculated photoconversion efficiency as a function of applied voltage, (C) J–V behavior under chopped light illumination, (D) amperometric I–t curves at a potential of 0.6 V under chopped light illumination, (E) IPCEs measured at an applied voltage of 0.6 V, and (F) electrochemical impedance spectra (EIS) measured at −0.4 V under illumination for the samples of TiO_2, TiO_2/NiFe-LDH, TiO_2/rGO, and TiO_2/rGO/NiFe-LDH NAs, respectively.

2636 | Energy Environ. Sci., 2016, 9, 2633–2643

This journal is © The Royal Society of Chemistry 2016

TiO$_2$/rGO, and TiO$_2$/rGO/NiFe-LDH NAs indicate a fast surface oxidation kinetics, suppressed electron–hole recombination[11,16] and excellent photochemical stability.

The influence of the rGO amount on the PEC performance of the TiO$_2$/rGO NAs was investigated. The rGO loading was tuned by changing the spin-coating cycles of GO solution onto TiO$_2$ NAs (denoted as TiO$_2$/rGO-x, where x is the cycle number of spin-coating). The loading amount of rGO nanosheets enhances as the spin-coating cycle increases from 1 to 20 (Fig. S6, ESI†), with a gradual increment of C content revealed by EDX spectra (Fig. S7, ESI†). LSV measurements for these TiO$_2$/rGO-x photoanodes show that the photocurrent density gradually increases at first from $x = 1$ to $x = 5$, and then decreases with the further enhancement of x (Fig. S8, ESI†). It is found that the NiFe-LDH growth on the surface of TiO$_2$ can be tuned by changing the loading amount of rGO (Fig. S9, ESI†) or the electrosynthesis time of LDH (Fig. S10, ESI†). With a moderate rGO loading amount (TiO$_2$/rGO-5) and electrodeposition time (50 s), NiFe-LDH nanoplatelets uniformly deposit on the surface of TiO$_2$ nanorods. Therefore, the TiO$_2$/rGO-5 sample with the highest photocurrent density is chosen for further study.

In addition to the loading amount of rGO, the influence of the rGO position on the PEC performance of the TiO$_2$/rGO NAs was also investigated. A control sample with most rGO nanosheets covering the top of the TiO$_2$ NAs (denoted as TiO$_2$/rGO-cover, Fig. S11, ESI†) was prepared by drop-casting GO aqueous solution on TiO$_2$ NAs. The TiO$_2$/rGO-cover NA electrode exhibits an anodic shift for the onset potential (from -0.2 V to -0.1 V) and a decrease in photocurrent density (from 1.50 mA cm^{-2} to 1.14 mA cm^{-2} at 0.6 V) compared with the TiO$_2$/rGO NAs (Fig. S12A, ESI†). This can be attributed to the decreased charge separation and restrained contact between TiO$_2$ and the electrolyte owing to the intense coverage of rGO nanosheets (Fig. S12B and C, ESI†).

The incident photon-to-current conversion efficiency (IPCE) was measured to understand the relationship between the photocatalytic activity and light absorption. All these samples exhibit photocatalytic activity in the UV region (below 420 nm) and inactivity in the visible region (Fig. 3E). The maximum IPCEs are obtained at 400 nm, which are 2.77%, 3.40%, 4.44%, and 5.12% for TiO$_2$, TiO$_2$/NiFe-LDH, TiO$_2$/rGO and TiO$_2$/rGO/NiFe-LDH NAs, respectively. The largely enhanced IPCE of the TiO$_2$/rGO/NiFe-LDH NAs further confirms the integrated contribution of rGO and NiFe-LDH to the PEC performance. In addition, the profiles of all these IPCE curves are consistent with the UV-Vis absorption spectrum of TiO$_2$, indicating that only TiO$_2$ acts as a UV light responsive photocatalyst, and the visible light absorption by rGO and NiFe-LDH cannot drive the PEC water splitting. To further obtain the oxygen production quantum efficiency, the produced oxygen over TiO$_2$/rGO/NiFe-LDH photoanodes by chronoamperometry with monochromatic irradiation was monitored. As shown in Fig. S13 (ESI†), the oxygen production quantum efficiency ($\sim$5.07% at 400 nm) shows a high accordance with the IPCE result (5.12% at 400 nm).

Electrochemical impedance spectroscopy (EIS) studies were carried out to investigate the charge transport behavior in these photoanodes. As shown in Fig. 3F, the ternary TiO$_2$/rGO/NiFe-LDH NAs display the smallest charge transfer resistance (corresponding to the semicircle diameter in the plot) among these four samples, indicating the fastest charge transport kinetics. Moreover, a larger slope of the straight line is observed for the TiO$_2$/rGO/NiFe-LDH NAs than that of the TiO$_2$/rGO NAs, suggesting the enhanced mass transfer kinetics on the electrode/electrolyte interface.[15,28] This is attributed to the hierarchical NiFe-LDH shell which provides sufficient surface active sites and porous structures for ion diffusion and oxygen escape.

In order to confirm the products of anodic photocurrent in these photoanodes, both the photocurrent and the produced O$_2$ were monitored during the bulk electrolysis measurements (Fig. S14, Fig. 4A, and Table S3, ESI†). By comparing the theoretical O$_2$ production calculated from the photocurrent
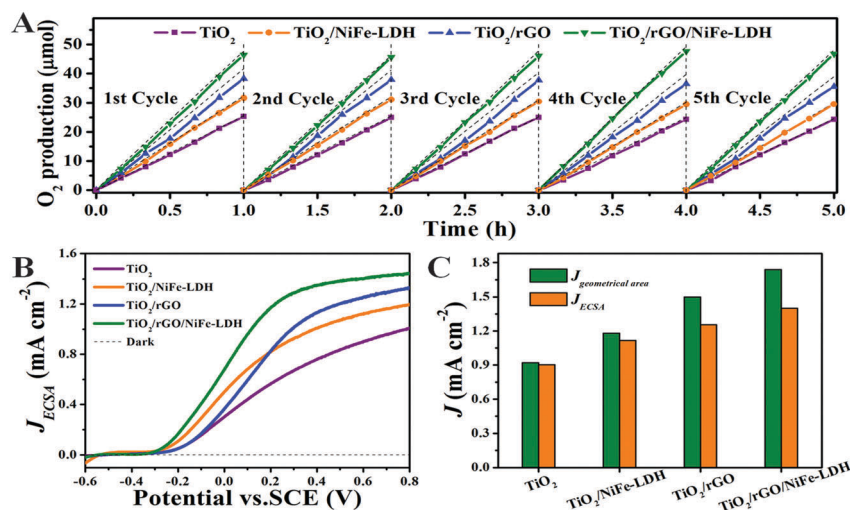

Fig. 4 (A) Total O$_2$ production detected by a gas chromatograph (the dashed lines are the theoretical O$_2$ production calculated from the measured photocurrent assuming 100% faradaic efficiency), (B) ECSA normalized photocurrent density vs. voltage curves, and (C) a comparison of the photocurrent density normalized by the geometrical area and the ECSA at 0.6 V for TiO$_2$, TiO$_2$/NiFe-LDH, TiO$_2$/rGO, and TiO$_2$/rGO/NiFe-LDH NAs, respectively.

with the actual O_2 yield, the average faradaic efficiency is obtained, which is 98%, 97%, 92%, and 97% for TiO_2, TiO_2/NiFe-LDH, TiO_2/rGO, and TiO_2/rGO/NiFe-LDH, respectively. These very high photocurrent-to-oxygen conversion efficiencies indicate successful water splitting during the PEC reaction. In addition, the TiO_2/rGO/NiFe-LDH photoanode shows an average O_2 production of 15.5 µmol h^{-1} cm^{-2}, which is 1.25, 1.52 and 1.88 times larger than that of TiO_2/rGO, TiO_2/NiFe-LDH and pristine TiO_2, respectively. This confirms that the introduction of rGO and NiFe-LDH indeed enhances the PEC water oxidation. The subtle difference between the theoretical O_2 production and the actual O_2 yield is likely due to a small amount of gas leakage or oxygen reduction on the Pt electrodes.[10]

It has been reported that rGO is oxidatively photodegraded in some semiconductor/rGO composites during long-time irradiation due to the accumulation of photogenerated holes.[28,46] In this work, the oxygen production of the TiO_2/rGO photoanode shows a decline of 7% within 5 cycles (Table S3: 5×1 h, ESI†); the faradaic efficiency of TiO_2/rGO ($\sim$92%) also shows a decrease compared with that of pristine TiO_2 ($\sim$98%). These observations indicate a slight oxidation of rGO in TiO_2/rGO NAs.

In contrast, the TiO_2/rGO/NiFe-LDH photoanode exhibits a rather stable oxygen production without any decay within 5 cycles, and the faradaic efficiency remains at 97% (Table S3, ESI†). The C 1s XPS spectra of fresh TiO_2/rGO (Fig. S15, curve a, ESI†) and TiO_2/rGO/NiFe-LDH (Fig. S15, curve c, ESI†) show typical C states in rGO with binding energies of 284.8, 285.9, 287.1 and 288.6 eV for C–C, C–O, C=O and COO, respectively.[47] After a 5 h chronoamperometry measurement, the chemical state of C in TiO_2/rGO (Fig. S15, curve b, ESI†) and TiO_2/rGO/NiFe-LDH (Fig. S15, curve d, ESI†) does not show any change. The intensity of the C 1s peak of TiO_2/rGO displays a slight decrease, implying the photodegradation of rGO. However, the TiO_2/rGO/NiFe-LDH sample shows a rather steady C 1s peak intensity after long term test, demonstrating satisfactory stability of rGO in the ternary TiO_2/rGO/NiFe-LDH system. The enhanced stability can be attributed to efficient water oxidation catalyzed by NiFe-LDH, which suppresses the accumulation of photogenerated holes on the surface of the electrodes.

To understand the intrinsic PEC activity of these photoanodes, we normalized the photocurrent by the electrochemically active surface area (ECSA) estimated from the double-layer capacitance (C_{dl}) of the electrode surface.[48,49] As a result, the ECSA was calculated to be 3.08, 3.16, 3.58, and 3.72 cm^2 for TiO_2, TiO_2/NiFe-LDH, TiO_2/rGO and TiO_2/rGO/NiFe-LDH, respectively (Fig. S16–S18; see detailed calculation in the ESI†). The LSV curve for PEC water splitting is normalized by the ECSA of each sample (Fig. 4B). It is found that the photocurrent densities normalized to the ECSA for these four photoanodes are correspondingly lower than those normalized to the geometrical area (Fig. 4C). Nevertheless, the overall improvement tendency of the PEC performance for these photoanodes is unchanged, indicating an enhanced intrinsic PEC activity by the introduction of rGO and NiFe-LDH to TiO_2.

The TiO_2/rGO/NiFe-LDH NA photoanode also exhibits excellent stability with negligible photocurrent decay (3%) after 3 h of

PEC water splitting reaction at 0.6 V (Fig. S19A, ESI†), which is among the highest performance of reported results.[15,16,20] In addition, the J–V curve of the TiO_2/rGO/NiFe-LDH NAs after this 3 h test does not show obvious change compared with the original sample (Fig. S19B, ESI†). The SEM image shows that the ordered array structure and the core–shell hierarchical morphology of the TiO_2/rGO/NiFe-LDH NAs remain unchanged after long-term measurement (Fig. S19C, ESI†); the EDX spectrum only displays a tiny decrease in the elemental content of Ni and Fe (Fig. S19D, ESI†). These results above confirm the stability of this TiO_2/rGO/NiFe-LDH photoanode. Moreover, this ternary electrode configuration is also effective for other semiconductor nanoarrays such as α-Fe_2O_3 and WO_3. With the co-decoration of rGO and NiFe-LDH, the resulting Fe_2O_3/rGO/NiFe-LDH and WO_3/rGO/NiFe-LDH NAs show largely enhanced PEC performances (with a 5.9 and 2.7 times enhancement of the photocurrent density relative to pristine Fe_2O_3 and WO_3 NAs at 0.8 V, respectively, as shown in Fig. S20, ESI†). The highly efficient improvement of the PEC behavior in these systems (TiO_2, α-Fe_2O_3, and WO_3) demonstrates the universality of this modification strategy for semiconductor photoanodes.

2.3 Mechanism discussion

All the above results demonstrate that rGO and NiFe-LDH can largely improve the PEC performance in the TiO_2 photoanode. To gain further insight into the mechanism of this synergistic effect, X-ray photoelectron spectroscopy (XPS) was performed to investigate the interaction and charge transfer in these hybrid NAs. Fig. 5A shows the Ti 2p XPS spectra, which are deconvoluted by the Ti $2p_{3/2}$ and Ti $2p_{1/2}$ peaks. For pristine TiO_2 NAs, the Ti^{4+} state is determined by the binding energies of 458.6 and 464.3 eV for Ti $2p_{3/2}$ and Ti $2p_{1/2}$, respectively.[50] After the incorporation of rGO, these two Ti 2p peaks increase to 459.1 eV and 464.8 eV (Fig. 5A, curve b). Moreover, the O 1s spectrum of the TiO_2 NAs is deconvoluted into two peaks at 529.9 and 531.6 eV (Fig. 5B), corresponding to oxygen (O^{2-}) in the lattice of TiO_2 and the surface absorbed OH group, respectively.[14] A positive shift of the O^{2-} peak (530.4 eV) is observed after the combination with rGO (Fig. 5B, curve b), accompanied with the oxygenic groups in rGO centered at 531.8 eV (COO), 532.5 eV (C=O), and 533.9 eV (C–OH).[47] The positive shift of the binding energies for both Ti 2p and O 1s indicates a decrease in the electron density of TiO_2. This can be ascribed to the surface binding interaction between TiO_2 and rGO, which induces an electron transfer from TiO_2 to rGO.[40] In contrast, the binding energies of Ti $2p_{3/2}$ and Ti $2p_{1/2}$ in the TiO_2/NiFe-LDH NAs show a negative shift to 458.2 and 463.8 eV, respectively (Fig. 5A, curve c), compared with those in the pristine TiO_2 NAs. This negative shift of the Ti 2p binding energies accompanied with the positive shift of the Fe 2p and Ni 2p binding energies (Fig. 5C and D, curve a) indicates an electron transfer from NiFe-LDH to TiO_2. Consequently, a combined effect of rGO and the NiFe-LDH shell on the TiO_2 core is reflected in the case of TiO_2/rGO/NiFe-LDH, giving rise to Ti 2p binding energies rather close to pristine TiO_2 (Fig. 5A, curve d).

The oxidation states of Ni and Fe in NiFe-LDH were also investigated (Fig. 5C and D); TiO_2/NiFe-LDH and TiO_2/rGO/NiFe-LDH NAs show the Ni^{2+} and Fe^{3+} oxidation states of a

2638 | *Energy Environ. Sci.,* 2016, **9**, 2633–2643

This journal is © The Royal Society of Chemistry 2016
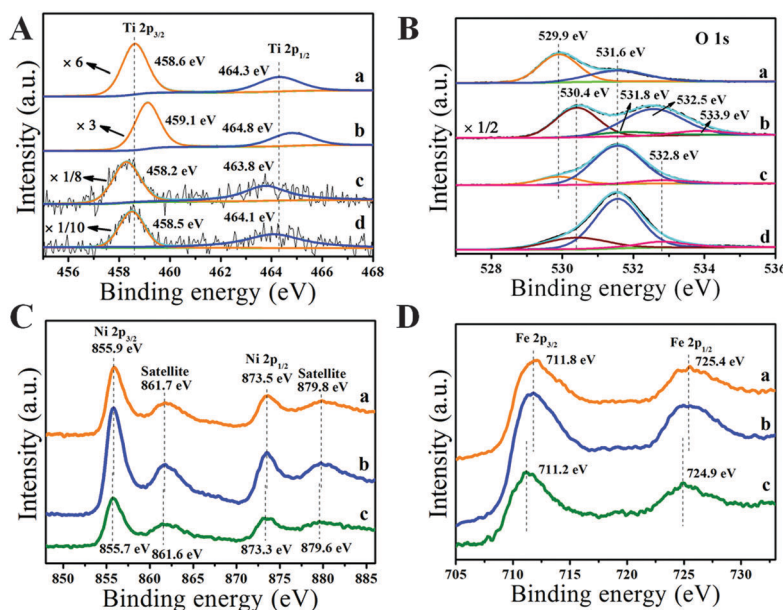
Fig. 5 (A) Ti 2p and (B) O 1s XPS spectra of (a) TiO$_2$, (b) TiO$_2$/rGO, (c) TiO$_2$/NiFe-LDH, and (d) TiO$_2$/rGO/NiFe-LDH NAs, respectively; (C) Ni 2p and (D) Fe 2p XPS spectra of (a) TiO$_2$/NiFe-LDH NAs, (b) TiO$_2$/rGO/NiFe-LDH NAs, and (c) NiFe-LDH nanoplatelet arrays directly electrodeposited on the FTO substrate.

typical LDH phase.[51,52] In addition, compared with the NiFe-LDH arrays (Fig. 5C and D, curve c), both TiO$_2$/NiFe-LDH and TiO$_2$/rGO/NiFe-LDH NAs display a positive shift in the Ni 2p and Fe 2p peaks (Fig. 5C and D, curve a and b), which further confirms the electron transfer from NiFe-LDH to TiO$_2$ in these two samples. This electron transfer process benefits electron–hole separation, which contributes to the largely enhanced PEC performance.

We use electrochemical impedance measurements to investigate the semiconducting properties of the obtained NAs. The positive slopes of the Mott–Schottky plots for all these samples indicate the n-type TiO$_2$ semiconductor (Fig. 6A). The charge carrier density is calculated from the slope according to the Mott–Schottky equation,[53] which is 1.89×10^{19}, 2.00×10^{19}, 4.36×10^{19}, and 3.32×10^{19} cm^{-3} for TiO$_2$, TiO$_2$/NiFe-LDH, TiO$_2$/rGO, and TiO$_2$/rGO/NiFe-LDH NAs, respectively. The very slight change of the charge carrier density indicates that the deposition of rGO and NiFe-LDH barely affects the doping level or carrier density of TiO$_2$. However, by extrapolating the Mott–Schottky plot to $1/C^2 = 0$ to obtain the intercept, the flat band potential is obtained, which exhibits an evidently positive shift after the electrodeposition of NiFe-LDH (Fig. 6A). The positive shift of the flat band potential for TiO$_2$ suggests a decrease in the bending of the band edges, which is attributed to the facilitated electrode/electrolyte interface charge transfer.[7,53] This result confirms the contribution of NiFe-LDH to the improved surface reaction kinetics.

The charge separation efficiency and surface charge injection efficiency were obtained by a comparison study between the photocurrent density originating from oxidizing H$_2$O and Na$_2$SO$_3$ as well as the theoretical maximum photocurrent density (see detailed discussions in the ESI†).[11,16,54,55] The results are shown in Fig. S21 (ESI†) and the calculated charge separation and charge injection efficiency are displayed in Fig. 6B and C, respectively. According to the IPCE results, only TiO$_2$ serves as the photocatalyst which converts absorbed UV light to photocurrent in these four photoanodes (TiO$_2$, TiO$_2$/NiFe-LDH, TiO$_2$/rGO, and TiO$_2$/rGO/NiFe-LDH); moreover, they show rather similar absorbance in the UV region (Fig. 2C). Therefore, the theoretical photocurrent density ($J_{absorbed}$) of TiO$_2$ is used to calculate the charge separation and charge injection efficiency. A largely enhanced charge separation efficiency (98% at 0.6 V) is observed in TiO$_2$/rGO and TiO$_2$/rGO/NiFe-LDH NAs relative to NAs without rGO (66% at 0.6 V). However, only a slight change in the charge separation efficiency is observed along with the incorporation of NiFe-LDH in TiO$_2$/rGO NAs. This indicates that the bulk recombination of photogenerated electron–hole pairs is significantly suppressed via the incorporation of rGO. For the charge injection efficiency, a giant improvement is obtained (95% for TiO$_2$/NiFe-LDH and TiO$_2$/rGO/NiFe-LDH) with the integration of NiFe-LDH, suggesting its highly efficient catalytic activity toward water oxidation. In addition, the deposition of rGO on TiO$_2$ NAs also enhances the charge injection efficiency (from 75% to 82% at 0.6 V), which is mainly attributed to the suppressed surface electron–hole recombination by the electron transfer from TiO$_2$ to rGO. With the synergistic assistance of rGO and NiFe-LDH, the TiO$_2$/rGO/NiFe-LDH NA photoanode exhibits excellent charge separation and water oxidation performance, which achieves a $P_{\text{charge separation}} \times P_{\text{charge injection}}$ product of 93% at 0.6 V, much superior to those of previously reported TiO$_2$-based photoanodes (about 60%–85%).[34,55,56]

It is found that the TiO$_2$/rGO NAs exhibit the longest fluorescence lifetime and the highest charge carrier density, but not the best PEC water splitting performance. Actually, both the
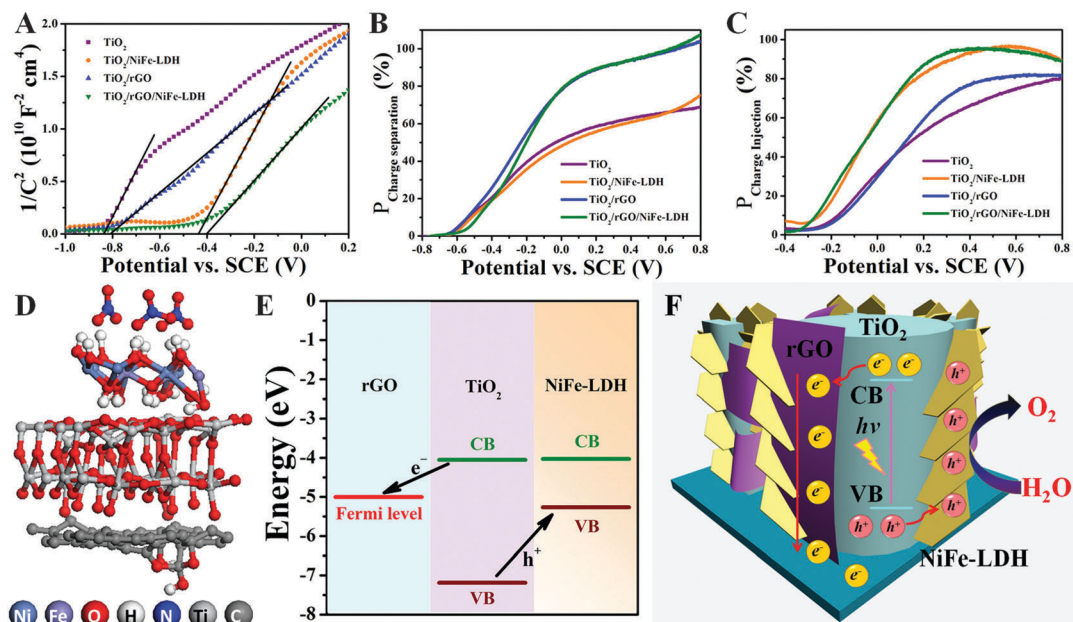
Fig. 6 (A) Mott−Schottky plots collected at a frequency of 1 kHz in the dark; (B) charge separation efficiency *vs.* potential curves and (C) charge injection efficiency *vs.* potential curves of TiO$_2$, TiO$_2$/NiFe-LDH, TiO$_2$/rGO, and TiO$_2$/rGO/NiFe-LDH NAs, respectively; (D) the optimized geometry of TiO$_2$/rGO/NiFe-LDH; (E) band edge placement of TiO$_2$, rGO and NiFe-LDH; (F) a schematic illustration of the PEC water oxidation process in the TiO$_2$/rGO/NiFe-LDH core−shell NA photoanode.

fluorescence lifetime and charge carrier density reflect the properties of charge carriers in the photoelectrode. The longest fluorescence lifetime of TiO$_2$/rGO than that of other samples indicates the remarkable contribution of rGO to the separation and migration of photogenerated charge carriers, which is consistent with the highest charge carrier density calculated from the Mott–Schottky plots. In addition to charge separation, the PEC water splitting performance of the photoanode is also dependent on the surface water oxidation reaction at the electrode/electrolyte interface. According to the charge injection efficiency data, NiFe-LDH serves as a highly-efficient water oxidation catalyst, accounting for the best PEC performance of TiO$_2$/rGO/NiFe-LDH NAs.

Density functional theory (DFT) with the Hubbard correction was employed to calculate the band edge placement of each component in TiO$_2$/rGO/NiFe-LDH. Detailed information on the model construction and the computational method is listed in the ESI† (Computational details and Fig. S22–S28, ESI†). The charge transfer between respective components is revealed based on their band edge position, which is calculated by using an individual model of each component. Moreover, we used a core–shell model of TiO$_2$/rGO/NiFe-LDH to better understand the interaction between the core (TiO$_2$) and the shell (rGO or NiFe-LDH) (Fig. 6D). The work function and band gap of the semiconductor were calculated to determine the conduction band minimum (CBM) and valence band maximum (VBM). The work function and band gap of TiO$_2$ are calculated to be 5.620 eV and 3.130 eV, respectively, very close to the reported values.[57] Accordingly, the CBM and VBM of TiO$_2$ are determined to be −4.053 eV and −7.187 eV relative to the vacuum level, respectively (Fig. 6E). By the same method, the work function

and band gap of NiFe-LDH are calculated to be 4.646 eV and 1.239 eV, which confirms its visible light absorption. The VBM of NiFe-LDH is located at −5.265 eV *vs.* the vacuum level, which is higher than that of TiO$_2$. This energy difference of the VBM triggers the transfer of photoinduced holes in TiO$_2$ to NiFe-LDH. On the other hand, the determined Fermi level of rGO is −5.006 eV, which is lower than the CBM of TiO$_2$. Therefore, the photogenerated electrons in the CB of TiO$_2$ tend to migrate to rGO. This electron–hole transfer based on the energy difference of the band edge position shows a high accordance with the XPS results. In addition, the binding energies of TiO$_2$/rGO and TiO$_2$/NiFe-LDH are calculated to be −22.881 eV and −20.496 eV, respectively, indicating a strong interaction between the core (TiO$_2$) and shell (rGO or NiFe-LDH).

Given the discussion above, a mechanism for the enhanced PEC water oxidation performance in this ternary TiO$_2$/rGO/NiFe-LDH NA photoanode is proposed and shown in Fig. 6F. Electron–hole pairs are firstly generated in TiO$_2$ under illumination. Based on the XPS analysis (Fig. 5) and DFT calculation (Fig. 6E), the band energy difference and chemical binding interaction between these components induce both electron transfer from TiO$_2$ to rGO and hole capture by NiFe-LDH. This opposite transmission of electrons and holes suppresses the surface recombination of photogenerated charge carriers. The rapid migration of electrons to the current collector was performed in rGO due to its superior electron mobility, which remarkably inhibits the bulk electron–hole recombination and enhances the charge separation efficiency. On the other hand, holes are captured by NiFe-LDH along with the oxidation of Fe, which acts as the active site for water oxidation.[58] Consequently, by the synergetic effect of rGO and NiFe-LDH, efficient PEC water

2640 | *Energy Environ. Sci.,* 2016, **9**, 2633–2643

This journal is © The Royal Society of Chemistry 2016

oxidation is performed in the ternary NAs with simultaneously improved charge separation and water oxidation efficiency.

3. Conclusions

In summary, well-aligned hierarchical TiO_2/rGO/NiFe-LDH NAs with a core–shell heterostructure have been successfully fabricated by a stepwise deposition of rGO and NiFe-LDH onto TiO_2 NAs. The resulting ternary NAs exhibit significantly enhanced efficiency in PEC water-splitting, including a large photocurrent and high stability. A deep insight into the mechanism for the enhanced PEC performance has also been studied carefully. The synergistic effect between rGO and NiFe-LDH simultaneously enhances the charge separation and water oxidation efficiency of the photoanodes. In addition, this modification approach can be extended to other semiconductor systems (α-Fe_2O_3 and WO_3). Therefore, this promising strategy can be used for the fabrication of novel photoelectrodes, which have potential applications in a variety of energy storage and conversion applications.

4. Experimental section

4.1   Preparation of TiO_2/rGO/NiFe-LDH NAs

The fabrication process of TiO_2/rGO/NiFe-LDH core–shell NAs is illustrated in Fig. 1A. Firstly, TiO_2 NAs were prepared on an FTO substrate *via* a previously reported hydrothermal method.[35] Typically, 12 mL of deionized water was mixed with 12 mL of concentrated hydrochloric acid (36.5–38 wt%); the mixture was stirred for 5 min, then 0.35 mL of titanium butoxide was added dropwise under continuous stirring. The resulting solution was transferred into a Teflon-lined stainless steel autoclave. One piece of cleaned FTO glass substrate (2 cm × 5 cm) was placed at an angle against the wall of the reactor with the conducting side facing down. Hydrothermal growth was performed at 150 °C for 20 h. After cooling down to room temperature, the FTO substrate was withdrawn, rinsed extensively with deionized water, and dried at 60 °C in air.

Graphite oxide (GO) was prepared *via* a modified Hummers' method.[59] Then the TiO_2/rGO NAs were prepared by a five-time spin-coating of a GO aqueous solution (0.2 mg mL^{-1}) onto the prepared TiO_2 NAs, followed by annealing at 450 °C in a N_2 atmosphere for 2 h to improve the adhesion between rGO and TiO_2. In this annealing process, GO was thermally reduced to rGO.

Electrochemical deposition of NiFe-LDH on TiO_2 and TiO_2/rGO NAs was performed in a three-electrode configuration by using TiO_2 NAs or TiO_2/rGO NAs as the working electrode, Pt wire as the counter electrode, and a saturated calomel electrode (SCE) as the reference electrode.[52] The electrolyte was obtained by dissolving 0.15 M of Ni(NO$_3$)$_2$·6H$_2$O and 0.15 M of FeSO$_4$·6H$_2$O in 50 mL of deionized water under stirring in a N_2 atmosphere to prevent the oxidation of Fe^{2+}. The potentiostatic deposition was carried out at a potential of −1.0 V *vs.* SCE for 50 s. The resulting NAs were withdrawn and rinsed with distilled water, and then were placed in ambient air for the self-oxidation of

Fe^{2+} to Fe^{3+}. By this method, TiO_2/NiFe-LDH and TiO_2/rGO/NiFe-LDH core–shell NAs were obtained. In addition, the preparation process of α-Fe_2O_3 and WO_3 nanowire arrays on the FTO substrate is described in the ESI.† The modification of rGO and NiFe-LDH on these nanowire arrays was performed by the same method used for TiO_2 NAs.

4.2   Characterization techniques

The morphology was investigated using a scanning electron microscope (SEM; Zeiss SUPRA 55) with an accelerating voltage of 20 kV combined with energy dispersive X-ray (EDX) spectroscopy. Transmission electron microscopy (TEM) images were recorded using a Hitachi H-800 TEM with an accelerating voltage of 200 kV. X-ray diffraction (XRD) patterns were collected on a Rigaku XRD-6000 diffractometer using Cu Kα radiation. Solid UV-vis diffuse reflection spectra were collected on a Shimadzu U-3000 spectrophotometer. Raman spectra were collected on a LabRAM ARAMIS Raman system using a 532 nm laser as the excitation source. Fluorescence spectra were recorded on a RF-5301PC fluorospectrophotometer with an excitation wavelength of 300 nm. Time-resolved photoluminescence spectra were recorded on a Edinburgh Instruments FL 900 fluorimeter with excitation and detection wavelength at 300 nm and 467 nm respectively. X-ray photoelectron spectra (XPS) were measured on a Thermo VG ESCALAB 250 X-ray photoelectron spectrometer using Al Kα radiation at a pressure of about 2×10^{-9} Pa.

4.3   Photoelectrochemical measurements

All PEC tests were performed on an electrochemical workstation (CHI 660e, CH Instruments Inc., Shanghai) in a three-electrode configuration with Pt wire as the counter electrode and SCE as the reference electrode. Measurements were performed in a neutral medium of a 0.5 M Na_2SO_4 aqueous solution (pH 6.8). The illumination source was a 150 W Xe lamp with a power density of 100 mW cm^{-2} on the photoanode. The as-obtained TiO_2, TiO_2/rGO, TiO_2/NiFe-LDH, and TiO_2/rGO/NiFe-LDH NAs on the FTO substrate were cut into slices with an area of 1 cm × 3 cm, followed by clamping a copper tape onto a bare part of the FTO substrate. The working, counter, and reference electrodes are installed in a quartz cell. The photocurrent was measured by linear sweep voltammetry at a scan rate of 10 mV s^{-1}. The photoconversion efficiency (η) was calculated using the following equation:

$$\eta = J \times (1.23 - E_{RHE})/P_{light} \tag{1}$$

where E_{RHE} is the applied bias *vs.* a reversible hydrogen electrode (RHE); J is the photocurrent density at the measured bias, and P_{light} is the irradiance intensity of 100 mW cm^{-2}. The E_{RHE} was calculated by:

$$E_{RHE} = E_{SCE} + E_{SCE}^{\theta} + 0.059 \times pH \tag{2}$$

where E_{SCE} is the applied bias *vs.* the SCE (which is the applied bias in this work) and E_{SCE}^{θ} is the standard electrode potential of the SCE (0.2438 V at 25 °C). The incident photon to current efficiency (IPCE) was evaluated at 0.6 V under monochromatic

light irradiation by using an optical filter on the Xe lamp. The IPCE was calculated using the equation:

$$\text{IPCE} = (1240 \times J_{\text{mono}})/(P_{\text{mono}} \times \lambda) \tag{3}$$

where J_{mono} is the measured photocurrent density at a specific wavelength; P_{mono} is the measured irradiance at a specific wavelength, and λ is the wavelength of incident light. Electrochemical impedance spectroscopy (EIS) was carried out by applying an AC voltage at -0.4 V in a frequency range from 100 kHz to 0.01 Hz under illumination. Mott–Schottky plots were evaluated at a DC potential range from -1.0 V to 0.2 V at a frequency of 1 kHz. The measurement of the photoelectrochemically generated O_2 was carried out in a home-made airtight transparent electrochemical cell (see the detailed description in the ESI†).

Acknowledgements

Notes and references

1 M. Gratzel, *Nature*, 2001, **414**, 338.
2 M. G. Walter, E. L. Warren, J. R. McKone, S. W. Boettcher, Q. Mi, E. A. Santori and N. S. Lewis, *Chem. Rev.*, 2010, **110**, 6446.
3 F. E. Osterloh, *Chem. Soc. Rev.*, 2013, **42**, 2294.
4 J. Yang, D. Wang, H. Han and C. Li, *Acc. Chem. Res.*, 2013, **46**, 1900.
5 T. Hisatomi, J. Kubota and K. Domen, *Chem. Soc. Rev.*, 2014, **43**, 7520.
6 X. Yu, X. Han, Z. Zhao, J. Zhang, W. Guo, C. Pan, A. Li and Z. L. Wang, *Nano Energy*, 2015, **11**, 19.
7 Y. Wang, Y. Y. Zhang, J. Tang, H. Wu, M. Xu, Z. Peng, X. G. Gong and G. Zheng, *ACS Nano*, 2013, **7**, 9375.
8 M. Xu, P. Da, H. Wu, D. Zhao and G. Zheng, *Nano Lett.*, 2012, **12**, 1503.
9 Z. Li, W. Luo, M. Zhang, J. Feng and Z. Zou, *Energy Environ. Sci.*, 2013, **6**, 347.
10 C. Du, X. Yang, M. T. Mayer, H. Hoyt, J. Xie, G. McMahon, G. Bischoping and D. Wang, *Angew. Chem., Int. Ed.*, 2013, **52**, 12692.
11 H. Dotan, K. Sivula, M. Grätzel, A. Rothschild and S. C. Warren, *Energy Environ. Sci.*, 2011, **4**, 958.
12 X. Liu, F. Wang and Q. Wang, *Phys. Chem. Chem. Phys.*, 2012, **14**, 7894.
13 X. Zhang, X. Lu, Y. Shen, J. Han, L. Yuan, L. Gong, Z. Xu, X. Bai, M. Wei, Y. Tong, Y. Gao, J. Chen, J. Zhou and Z. L. Wang, *Chem. Commun.*, 2011, **47**, 5804.
14 G. Wang, H. Wang, Y. Ling, Y. Tang, X. Yang, R. C. Fitzmorris, C. Wang, J. Z. Zhang and Y. Li, *Nano Lett.*, 2011, **11**, 3026.
15 Q. Liu, H. Lu, Z. Shi, F. Wu, J. Guo, K. Deng and L. Li, *ACS Appl. Mater. Interfaces*, 2014, **6**, 17200.
16 D. K. Zhong, S. Choi and D. R. Gamelin, *J. Am. Chem. Soc.*, 2011, **133**, 18370.
17 R. Liu, Z. Zheng, J. Spurgeon and X. Yang, *Energy Environ. Sci.*, 2014, **7**, 2504.
18 W. T. Sun, Y. Yu, H. Y. Pan, X. F. Gao, Q. Chen and L. M. Peng, *J. Am. Chem. Soc.*, 2008, **130**, 1124.
19 M. T. Mayer, C. Du and D. Wang, *J. Am. Chem. Soc.*, 2012, **134**, 12406.
20 P. M. Rao, L. Cai, C. Liu, I. S. Cho, C. H. Lee, J. M. Weisse, P. Yang and X. Zheng, *Nano Lett.*, 2014, **14**, 1099.
21 M. Li, K. Chang, T. Wang, L. Liu, H. Zhang, P. Li and J. Ye, *J. Mater. Chem. A*, 2015, **3**, 13731.
22 D. Chen, H. Zhang, Y. Liu and J. Li, *Energy Environ. Sci.*, 2013, **6**, 1362.
23 Y. H. Ng, A. Iwase, A. Kudo and R. Amal, *J. Phys. Chem. Lett.*, 2010, **1**, 2607.
24 Y. H. Ng, I. V. Lightcap, K. Goodwin, M. Matsumura and P. V. Kamat, *J. Phys. Chem. Lett.*, 2010, **1**, 2222.
25 N. Yang, J. Zhai, D. Wang, Y. Chen and L. Jiang, *ACS Nano*, 2010, **2**, 887.
26 L. Liu, Z. Liu, A. Liu, X. Gu, C. Ge, F. Gao and L. Dong, *ChemSusChem*, 2014, **7**, 618.
27 Q. Xiang, J. Yu and M. Jaroniec, *J. Am. Chem. Soc.*, 2012, **134**, 6575.
28 Y. Hou, F. Zuo, A. Dagg and P. Feng, *Nano Lett.*, 2012, **12**, 6464.
29 W. Li, S. W. Sheehan, D. He, Y. He, X. Yao, R. L. Grimm, G. W. Brudvig and D. Wang, *Angew. Chem., Int. Ed.*, 2015, **54**, 11428.
30 E. M. Steinmiller and K. S. Choi, *Proc. Natl. Acad. Sci. U. S. A.*, 2009, **106**, 20633.
31 W. D. Chemelewski, H. C. Lee, J. F. Lin, A. J. Bard and C. B. Mullins, *J. Am. Chem. Soc.*, 2014, **136**, 2843.
32 M. Gong, Y. Li, H. Wang, Y. Liang, J. Z. Wu, J. Zhou, J. Wang, T. Regier, F. Wei and H. J. Dai, *J. Am. Chem. Soc.*, 2013, **135**, 8452.
33 X. Long, J. Li, S. Xiao, K. Yan, Z. Wang, H. Chen and S. Yang, *Angew. Chem., Int. Ed.*, 2014, **53**, 7584.
34 X. Chang, T. Wang, P. Zhang, J. Zhang, A. Li and J. Gong, *J. Am. Chem. Soc.*, 2015, **137**, 8356.
35 B. Liu and E. S. Aydil, *J. Am. Chem. Soc.*, 2009, **131**, 3985.
36 W. He, Y. Yang, L. Wang, J. Yang, X. Xiang, D. Yan and F. Li, *ChemSusChem*, 2015, **8**, 1568.
37 M. Ye, D. Zheng, M. Wang, C. Chen, W. Liao, C. Lin and Z. Lin, *ACS Appl. Mater. Interfaces*, 2014, **6**, 2893.
38 Q. Huang, S. Tian, D. Zeng, X. Wang, W. Song, Y. Li, W. Xiao and C. Xie, *ACS Catal.*, 2013, **3**, 1477.
39 B. Li, Y. Zhao, S. Zhang, W. Gao and M. Wei, *ACS Appl. Mater. Interfaces*, 2013, **5**, 10233.
40 M. S. Sher Shah, A. R. Park, K. Zhang, J. H. Park and P. J. Yoo, *ACS Appl. Mater. Interfaces*, 2012, **4**, 3893.
41 Y. Lei, D. Zhang, G. W. Meng, G. H. Li, X. Y. Zhang, C. H. Liang, W. Chen and S. X. Wang, *Appl. Phys. Lett.*, 2001, **78**, 1125.
42 J. L. Gunjakar, T. W. Kim, H. N. Kim, I. Y. Kim and S. J. Hwang, *J. Am. Chem. Soc.*, 2011, **133**, 14998.

43 D. Zhang, C. Pang and X. Wang, *Chem. Commun.*, 2015, **51**, 17467.

44 L. Mohapatra and K. M. Parida, *Phys. Chem. Chem. Phys.*, 2014, **16**, 16985.

45 F. Dong, Z. Zhao, T. Xiong, Z. Ni, W. Zhang, Y. Sun and W. K. Ho, *ACS Appl. Mater. Interfaces*, 2013, **5**, 11392.

46 C. Liu, Y. Teng, R. Liu, S. Luo, Y. Tang, L. Chen and Q. Cai, *Carbon*, 2011, **49**, 5312–5320.

47 Y. Wang, Y. Shao, D. W. Matson, J. Li and Y. Lin, *ACS Nano*, 2010, **4**, 1790.

48 P. Waszczuk, P. Zelenay and J. Sobkowski, *Electrochim. Acta*, 1995, **40**, 1717.

49 C. C. L. McCrory, S. Jung, J. C. Peters and T. F. Jaramillo, *J. Am. Chem. Soc.*, 2013, **135**, 16977.

50 S. D. Perera, R. G. Mariano, K. Vu, N. Nour, O. Seitz, Y. Chabal and K. J. Balkus, *ACS Catal.*, 2012, **2**, 949.

51 C. Tang, H. S. Wang, H. F. Wang, Q. Zhang, G. L. Tian, J. Q. Nie and F. Wei, *Adv. Mater.*, 2015, **27**, 4516.

52 Z. Li, M. Shao, H. An, Z. Wang, S. Xu, M. Wei, D. G. Evans and X. Duan, *Chem. Sci.*, 2015, **6**, 6624.

53 W. Li, P. Da, Y. Zhang, Y. Wang, X. Lin, X. Gong and G. Zheng, *ACS Nano*, 2014, **8**, 11770.

54 A. Murphy, P. Barnes, L. Randeniya, I. Plumb, I. Grey, M. Horne and J. Glasscock, *Int. J. Hydrogen Energy*, 2006, **31**, 1999.

55 P. Yan, G. Liu, C. Ding, H. Han, J. Shi, Y. Gan and C. Li, *ACS Appl. Mater. Interfaces*, 2015, **7**, 3791.

56 W. Yang, Y. Yu, M. B. Starr, X. Yin, Z. Li, A. Kvit, S. Wang, P. Zhao and X. Wang, *Nano Lett.*, 5015, **15**, 7574.

57 R. Memming, *Semiconductor Electrochemistry*, Wiley-VCH, Weinheim, Germany, 1st edn, 2001, p. 105.

58 D. Friebel, M. W. Louie, M. Bajdich, K. E. Sanwald, Y. Cai, A. M. Wise, M. J. Cheng, D. Sokaras, T. C. Weng, R. Alonso-Mori, R. C. Davis, J. R. Bargar, J. K. Norskov, A. Nilsson and A. T. Bell, *J. Am. Chem. Soc.*, 2015, **137**, 1305.

59 W. S. Hummers and R. E. Offeman, *J. Am. Chem. Soc.*, 1958, **80**, 1339.